A global DIC algorithm for tracking rotating objects using image unwrapping and FFT analysis

A global DIC algorithm for tracking rotating objects using image unwrapping and FFT analysis

Abstract: Digital Image Correlation applied to rotating objects is a challenging task due to the extremely large displacements to be detected and to the rotation of the subsets during revolutions. For these reasons, conventional DIC algorithms are limited to about 7° rotations before losing tracking capabilities. Nevertheless, a full 360° rotation is to be tracked in practical scenarios, so that a new paradigm in optical tracking of rotating objects remains urgent. In this paper, a global DIC algorithm is proposed to overcome the limitations of conventional methods. A simple analytical representation of the roto-translation is proposed, and an optimization algorithm is developed to find the rotation angle and center to minimize the discrepancies between the reference and rotated image. The critical issue of the procedure is represented by the selection of a reliable first guess, which, due to the presence of several local minima and a really sharp global minimum, needs to be extremely accurate for the optimization to converge. To this extent, a robust procedure is proposed based on image unwrapping and spatial-FFT analysis of the unwrapped image to infer a reliable first guess to be fed to the subsequent final optimization process. The approach was validated through experimental analysis of a rotating PC fan.

Keywords: *Digital Image Correlation, Rotating DIC, Blisk measurements, Optical vibration measurements, image unwrapping*

*Corresponding author:

1. Introduction

A clear understanding of the dynamic behavior of rotating machinery is essential in the field of rotor dynamics, particularly for accurately characterizing the evolution of modal parameters, such as natural frequencies and damping ratios, as a function of rotational speed. Gyroscopic effects and centrifugal stiffening play a critical role in shaping the vibratory response of rotating systems. As the rotational speed increases and approaches the critical speed of the structure, the likelihood of resonance-induced failures rises significantly. Therefore, accurate consideration of these dynamic effects is essential to ensure the safe, efficient, and reliable operation of rotating machinery, making them a central focus in both design methodologies and condition monitoring practices [1]. Traditionally, contact-based methods (e.g., strain gauges) and optical techniques, such as Scanning Laser Doppler Vibrometry (SLDV) [2-7] and stereo-photogrammetry [8-11], have been employed to characterize vibratory responses. However, limitations related to durability, spatial resolution, mechanical complexity, and robustness, have pushed research interests towards the use of 3D Digital Image Correlation (3D-DIC). This non-contact, full-field measurement technique offers improved spatial coverage and robustness, making it a promising alternative for analyzing the dynamic response of rotating components [12, 13]. 3D-DIC is well established in the analysis of non-rotating systems and offers excellent spatial resolution. However, its direct application to rotating systems remains challenging due to the algorithmic limitations when large rotational displacements are involved. In particular, conventional DIC algorithms tend to fail when rotation angles exceed approximately 7°, as the reference-deformed image correlation breaks down [13, 14]. To face this issue, genetic algorithms have been experimented to obtain suitable initial estimates of displacement parameters [15, 16]. These methods are globally optimal but are characterized by high computational costs. An alternative can be represented by using incremental DIC approaches, where the reference image is periodically updated once the measurable angular limit is reached. This strategy has enabled successful experimental modal analyses on rotating tires [17] and disks [18]. However, such incremental updates introduce a new challenge: the accumulation of tracking errors over time. Even small mismatches between successive updates propagate, leading to a gradual drift in the rotation estimation. Furthermore, when fast rotations occur, the required update frequency becomes high, thus increasing computational cost and requiring high-performance cameras. To address this, several studies have proposed strategies to reduce cumulative error [19], and recent efforts have focused on enhancing the accuracy of initial displacement estimation in DIC pipelines. In this regard, directional DIC has been proposed as a viable alternative to conventional DIC, thus overcoming limitations in scenarios where image texture is not sufficient. Directional DIC incorporates prior knowledge or assumptions about the expected direction of motion in the image subset to be analyzed [20]. This approach is well-suited for rotating targets, where the knowledge of rotation parameters helps the initial estimation of the subset position. The ring projection scheme can be used to extract the rotation-invariant features of a template thus obtaining integer-pixel initial estimation of large rotation

parameters [21-23]. The technique uses a circular window to extract information from images so that no information changes before and after rotation. A local ring pattern, invariant to target rotation, is also used in [24] to convert the 2D template into a 1D gray value sequence along a circle and calculate correlation. In [25], an iterative angle compensation strategy is proposed to progressively refine the initial rotation estimation obtained by the Speeded-Up Robust Features (SURF) method. A rotation-invariant template, based on concentric rings, is used to evaluate the similarity between matched feature points. Polar-coordinates DIC formulations have been also proposed in order to inherently be more robust to large rotations [26].

Most of the above-presented approaches, however, rely on local approaches, either feature-based or subset-based, rather than purely global approaches. This means that, without global constraints, they are more prone to mismatches and inconsistencies, particularly when large rotations are involved. A reliable initial estimation of the rotation parameters is also required to prevent the convergence into local minima.

The work presented in this paper proposes a novel global DIC approach aimed at identifying the rigid-body displacement of a rotating object. Unlike incremental techniques that rely on frequent reference updates and suffer from cumulative tracking errors, the proposed method estimates the global roto-translation parameters through a Gauss-Newton optimization algorithm, which minimizes pixel-wise correlation errors across the whole image or selected image regions. To enhance computational efficiency, the algorithm incorporates a sensitivity-based pixel selection strategy, retaining only the most informative pixels, typically located along speckle edges, while discarding those in uniform regions that contribute little to displacement analysis. The method also overcomes the limitations of conventional DIC algorithms that fail beyond ~7° of rotation and avoids the high computational cost of genetic algorithms. By leveraging circular image unwrapping and spatial-domain FFT analysis, the approach transforms rotational motion into linear displacement, enabling robust initial parameter estimation. Compared to local or feature-based methods, which are sensitive to texture and prone to mismatches, the global formulation ensures consistency and accuracy even under large angular displacements. The integration of a row-wise FFT-based periodicity metric further enables reliable estimation of the center of rotation, addressing a critical challenge in rotation tracking. The proposed approach has been validated by measuring the rotational motion of a commercial PC fan, demonstrating a highly effective solution for full-field optical measurement of rotating structures, with potential applications in vibration analysis and modal characterization of rotating machinery.

2. Algorithm description

The objective of tracking a rotating body in a scene was divided into several sub-steps:

1) The roto-translation transformation was parametrized in order to derive an analytical model (Section 2.1);

2) The optimization problem was formalized to determine the roto-translation parameters that best match the reference and the rotated image (Section 2.2);
3) The definition of the initial guess for the optimization problem was divided into two tasks, both based on circular unwrapping of the image:
    a. An initial estimate of the center of rotation was obtained by maximizing the main spatial harmonic component in the unwrapped image (Section 2.7);
    b. The rotation angle was preliminarily estimated by applying a frequency-domain DIC algorithm to the same unwrapped image (Section 2.6).

It should be emphasized that, since optimization must be performed at each stage, it is crucial to compute the derivatives of each objective function with respect to the optimization parameters, in order to ensure both accuracy and computational efficiency. In the following, a practical case study is presented to illustrate the main challenges and results. The test images capture a rotating PC fan with seven blades, as shown in Fig. 1. Further details of the experimental setup are provided in Section 3.1.

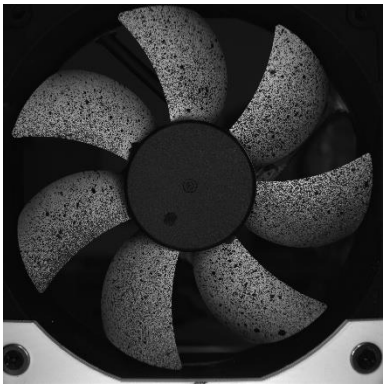

Figure 1 – Sample image from the dataset, used to discuss the main issues of the optimization process.

2.1. Roto-translation analytical formulation

One of the main challenges in tracking the motion of rotating structures with conventional Digital Image Correlation (DIC) algorithms is their limited ability to handle large subset rotations. Traditional DIC methods compute correlation by comparing image subsets along fixed horizontal and vertical directions (i.e., rows and columns). Consequently, their performance degrades significantly when the structure undergoes substantial rotation, since the subsets cannot be properly aligned between frames. To overcome this limitation, the present work employs a global DIC formulation specifically designed for rigid-body rotation. The procedure consists of defining a grid of points on the reference image, applying a roto-translation to their coordinates, and then comparing the corresponding gray-level values in the reference and rotated images. Rotation tracking is deemed successful when a close agreement between gray levels is obtained. In cases where the motion is governed by a rigid roto-translation, the displacement of any pixel in the image can be fully described by only

three scalar parameters: the rotation angle θ and a two-dimensional translation vector T. Using these parameters, the transformed coordinates X_r of a point in the rotated image can be computed from its original coordinates X in the reference image, according to the following relation:

$$R = \begin{bmatrix} \cos(\theta) & -\sin(\theta) \\ \sin(\theta) & \cos(\theta) \end{bmatrix}$$
$$X_r = RX + T \tag{1}$$

Where R is the two-dimensional rotation matrix and T is the translation vector. In the case of a rigid rotation, the center of rotation C remains invariant, i.e., $C_r = C$. This property allows the translation vector T to be directly related to the position of the center of rotation through the following expression:

$$C_r = RC + T = C \rightarrow T = (E - R)C \tag{2}$$

The matrix E in Eq. 2 represents the 2×2 identity matrix.

Since general roto-translations map pixel coordinates to non-integer positions, it is not possible to directly retrieve the corresponding gray-level values in the rotated image. To address this, an interpolation scheme such as bicubic spline interpolation, as proposed in [27], can be used to estimate gray levels at subpixel locations with high accuracy. For a given roto-translation, the interpolated gray levels of the rotated image at the transformed coordinates are collected in a column vector I_q. These values are then compared with the original intensities in the reference image, arranged in a column vector I_0, allowing the computation of a pixel-wise intensity error over the entire image or within a selected region of interest (ROI). Figure 2 illustrates this procedure for a generic pixel, highlighting the comparison between reference and transformed intensities.

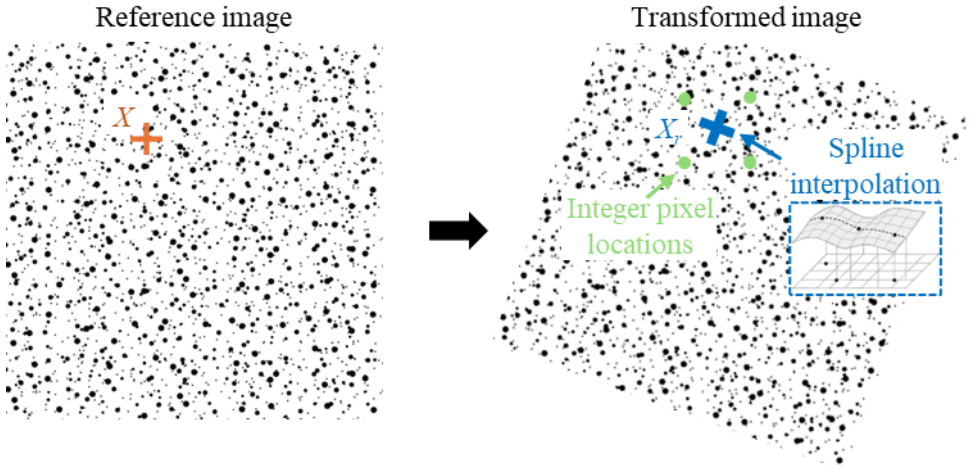

Figure 2 – Interpolation scheme to assess gray levels at non-integer pixel locations after roto-translation.

It should be emphasized that the roto-translation parameters θ and T are not known a priori and must be estimated. To this end, a set of pixels is selected for tracking. These pixels do not need to belong to a regular

grid and can be freely and non-uniformly distributed across the reference image. An optimization procedure is then employed to determine the values of θ and T that minimize the difference between the reference image and the interpolated transformed image, i.e., $e = I_0 - I_q$. This approach effectively aligns the images despite rotation and enables reliable motion tracking of rotating structures even under large angular displacements.

2.2. Gauss-Newton optimization scheme

The procedure described above is inherently non-linear, mainly due to the use of spline interpolation and the trigonometric functions in the transformation model (see Eq. 1). Nevertheless, the problem can be effectively addressed using the Gauss–Newton optimization method [28, 29]. This iterative scheme is well-suited for non-linear least-squares problems, as it minimizes the objective function by exploiting the gradient (Jacobian) of the error with respect to the optimization variables. In this case, the optimization variables are the rotation angle θ and the translation vector T, while the objective function is defined as the pixel-wise intensity difference between the reference image and the transformed (rotated and translated) image. The computation of the gradients required by the Gauss–Newton method is carried out in three main steps. Let $X_{r,1}$ and $X_{r,2}$ denote the horizontal and vertical components of the rotated coordinates X_r, respectively, and let T_1 and T_2 be the corresponding components of the translation vector T. Moreover, define R_1 and R_2 as the first and second rows of the rotation matrix R introduced in Eq. 1. The derivatives of the rotated coordinates with respect to the optimization variables θ, T_1 and T_2 can then be expressed analytically as:

$$\begin{gathered}\frac{\partial R_1}{\partial \theta} = [-\sin(\theta) \quad -\cos(\theta)];\ \frac{\partial R_2}{\partial \theta} = [\cos(\theta) \quad -\sin(\theta)] \\ \frac{\partial \mathrm{X}_{\mathrm{r},1}}{\partial \theta} = \frac{\partial R_1}{\partial \theta} X;\ \frac{\partial \mathrm{X}_{\mathrm{r},2}}{\partial \theta} = \frac{\partial R_2}{\partial \theta} X \\ \frac{\partial \mathrm{X}_{\mathrm{r},1}}{\partial \mathrm{T}_1} = 1;\ \frac{\partial \mathrm{X}_{\mathrm{r},2}}{\partial \mathrm{T}_1} = 0 \\ \frac{\partial \mathrm{X}_{\mathrm{r},1}}{\partial \mathrm{T}_2} = 0;\ \frac{\partial \mathrm{X}_{\mathrm{r},2}}{\partial \mathrm{T}_2} = 1\end{gathered} \tag{3}$$

Since the gray-level values I_q are evaluated at the transformed coordinates X_r, their derivatives with respect to the spatial coordinates are given by $\frac{\partial I_q}{\partial X_{r,1}}$ and $\frac{\partial I_q}{\partial X_{r,2}}$. These spatial gradients can be computed using the formulation reported in [27] (Eq. 5), and are readily available from the bicubic interpolation scheme. The residual error to be minimized is defined as $e = I_0 - I_q$. Since the reference image I_0 does not vary with respect to the optimization parameters, its derivative is zero. Consequently, the complete derivative of the error e with

respect to θ and T depends solely on the derivatives of I_q. Applying the chain rule, the total derivatives can be expressed as:

$$\frac{\partial e}{\partial \theta} = -\frac{\partial I_q}{\partial \theta} = -\left(\frac{\partial I_q}{\partial X_{r,1}}\frac{\partial X_{r,1}}{\partial \theta} + \frac{\partial I_q}{\partial X_{r,2}}\frac{\partial X_{r,2}}{\partial \theta}\right)$$

$$\frac{\partial e}{\partial T_1} = -\frac{\partial I_q}{\partial T_1} = -\left(\frac{\partial I_q}{\partial X_{r,1}}\frac{\partial X_{r,1}}{\partial T_1} + \frac{\partial I_q}{\partial X_{r,2}}\frac{\partial X_{r,2}}{\partial T_1}\right) \quad (4)$$

$$\frac{\partial e}{\partial T_2} = -\frac{\partial I_q}{\partial T_2} = -\left(\frac{\partial I_q}{\partial X_{r,1}}\frac{\partial X_{r,1}}{\partial T_2} + \frac{\partial I_q}{\partial X_{r,2}}\frac{\partial X_{r,2}}{\partial T_2}\right)$$

With these derivatives available, an iterative Gauss–Newton scheme can be employed to update the optimization parameters $v = [\theta, T_1, T_2]$ at each iteration. The update rule at iteration i can be written in compact form as:

$$J = \left[\frac{\partial I_q}{\partial \theta} \quad \frac{\partial I_q}{\partial T_1} \quad \frac{\partial I_q}{\partial T_2}\right]$$

$$v_{i+1} = v_i + (J^T J)^{-1} J^T e \quad (5)$$

This expression defines the recursive procedure used to progressively refine the estimates of the rotation and translation parameters until convergence. A common convergence criterion is based on the stagnation of the optimization parameters, i.e., when the relative change in the parameter vector between successive iterations (λ) falls below a user-defined threshold ε. This condition can be written as:

$$\lambda = \frac{||v_{i+1} - v_i||}{||v_i||} < \varepsilon \quad (6)$$

where $\| \cdot \|$ denotes the norm of the argument. This criterion ensures that the iterative process terminates once further updates no longer produce significant improvements in the estimated parameters.

2.3. Informative pixel selection

The error vector e in Eq. 5, in principle, can be computed on all pixels within a selected ROI to guide the optimization process and determine the optimal values of θ and T. Nevertheless, performing computations on the full set of pixels is highly inefficient, as it considerably increases the computational burden without providing additional benefits. In practice, only pixels located along the speckle edges are truly informative,

since their gray-level intensity is strongly affected by displacements. By contrast, pixels belonging to uniformly dark or bright regions contribute little to the analysis, as their intensity remains nearly constant under translation or rotation, and it is mostly affected by image noise. To systematically identify the most relevant pixels, the derivatives of I_q with respect to the optimization variables (see Eq. 4) were evaluated at each pixel. Based on these derivatives, a sensitivity parameter S_d ranging from 0 to 1 was introduced to quantify the responsiveness of individual pixels to roto-translational transformations:

$$S_d = \frac{1}{3}\left(\frac{\frac{\partial I_q}{\partial \theta}^2}{\max\left(\frac{\partial I_q}{\partial \theta}^2\right)} + \frac{\frac{\partial I_q}{\partial T_1}^2}{\max\left(\frac{\partial I_q}{\partial T_1}^2\right)} + \frac{\frac{\partial I_q}{\partial T_2}^2}{\max\left(\frac{\partial I_q}{\partial T_2}^2\right)} \right) \tag{7}$$

Pixels with larger S_d values are expected to provide more discriminative information, thereby playing a crucial role in the optimization procedure. In the present work, all the pixels having a value of S_d greater than the mean value of S_d were selected, which allowed for the extraction of the most informative pixels while discarding the redundant ones. The effect of this procedure is exemplified in Fig. 3. Figure 3(a) shows the value of S_d in the whole considered ROI with a color scale. The blade region depicted with a box in Fig. 3(a) was zoomed in Fig. 3(b), to highlight that the informative pixels are indeed the ones corresponding to the speckles' edge. As illustrated in Fig. 3, this strategy effectively reduces the dataset to approximately 30 % of the original number of pixels in the ROI. Such a reduction leads to a substantial decrease in computational cost, while enhancing the accuracy and robustness of the optimization results.

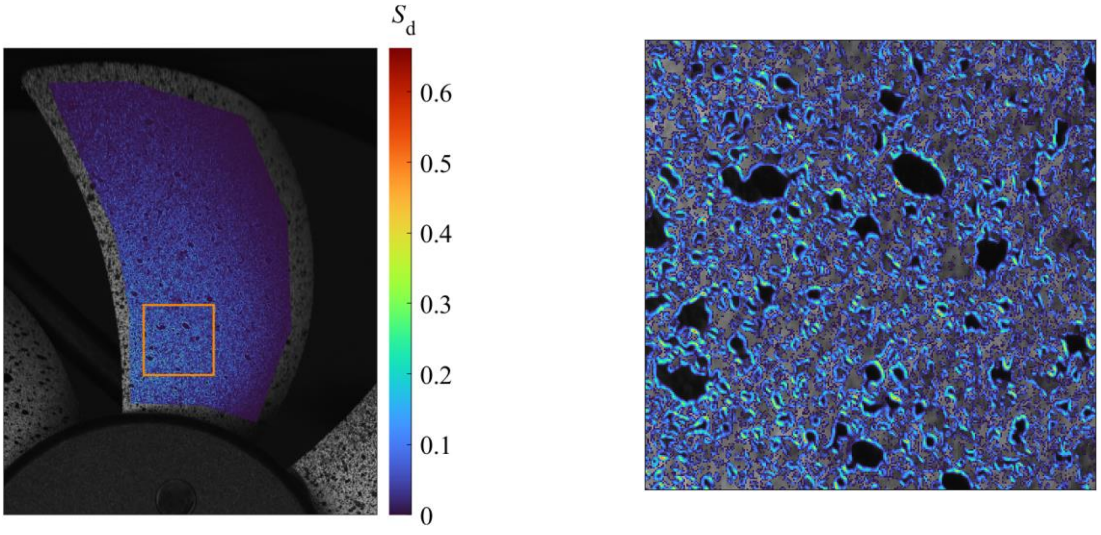

(a) (b)

Figure 3 – Selection of informative points: (a) distribution of the parameter S_d and (b) zoomed view of the region of the blade highlighted by the orange box.

2.4. Optimization space exploration

To gain further insight into the optimization problem, the rotating fan illustrated in Fig. 1 was analyzed. The fan was imaged at three different rotation angles with respect to a reference configuration, and the described procedure was applied by imposing tentative values of the optimization parameters and computing the corresponding residuals e. To represent the optimization function as a 3D surface, the scalar $e_n = ||e||/\sqrt{n_e}$ was introduced, where n_e denotes the number of elements in e. In this case, the optimal roto-translation parameters were identified through a trial-and-error strategy, repeating the optimization procedure with different initial guesses. A three-step process was adopted: (i) a tentative center of rotation was manually selected in the image; (ii) a *for-loop* search over the range 0–360° was performed with a step size of 0.5°, and the angle corresponding to the minimum e_n was selected; (iii) the optimization algorithm was then executed starting from this estimate to refine the solution and reach the global minimum. Although this procedure required significant computational effort (approximately 60 minutes per image), it enabled the determination of the optimal parameter $v_o = [\theta_o, T_{1,o}, T_{2,o}]$ for each of the three images. It was then possible to graphically represent the trends of e_n with respect to the optimization parameters. To reduce the dimensionality of the representation, the translation vector T was replaced by a scalar parameter ρ, defined as the distance between the tentative translation T_i at the i-th iteration and the optimal solution $T_o = [T_{1,o}, T_{2,o}]$. Furthermore, the two-dimensional translation space was explored only along the direction aligned with θ_o, according to the following relation:

$$T_i = [T_{1,i}, T_{2,i}] = T_o + \rho[\sin(\theta_o), \cos(\theta_o)] \tag{8}$$

This allowed to reduce the three-dimensional optimization space to a two-dimensional one, which can be easily visualized in a 3D plot as shown in Fig. 4(a). Subsequently, a fine grid of investigation points was defined to explore the selected range of the optimization variables (reduced to θ and ρ), and the corresponding values of $e_{n,i}$ were computed for each point. The results obtained for the first image are presented in Fig. 4(a).

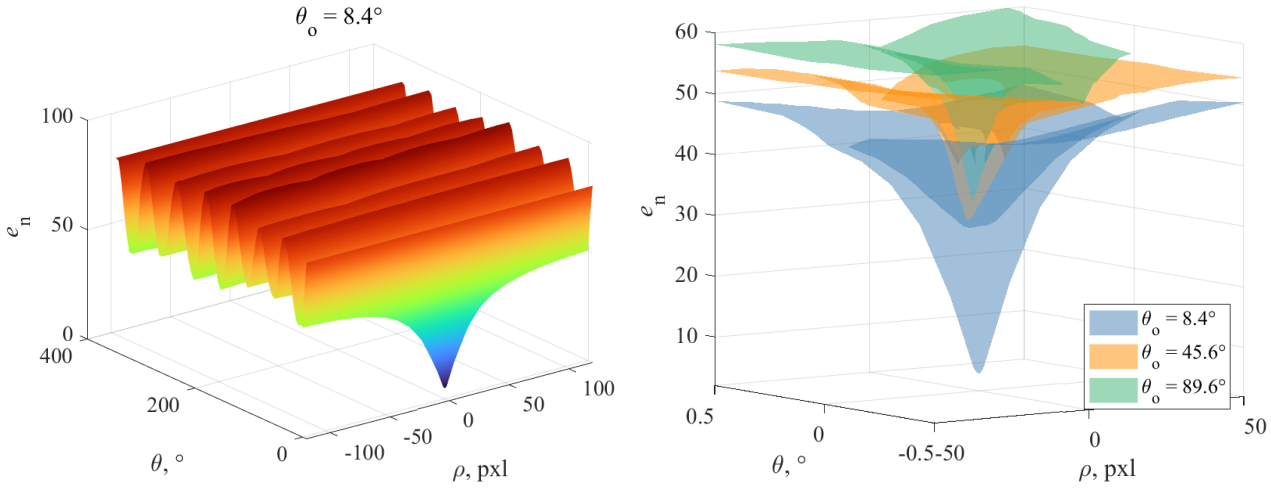

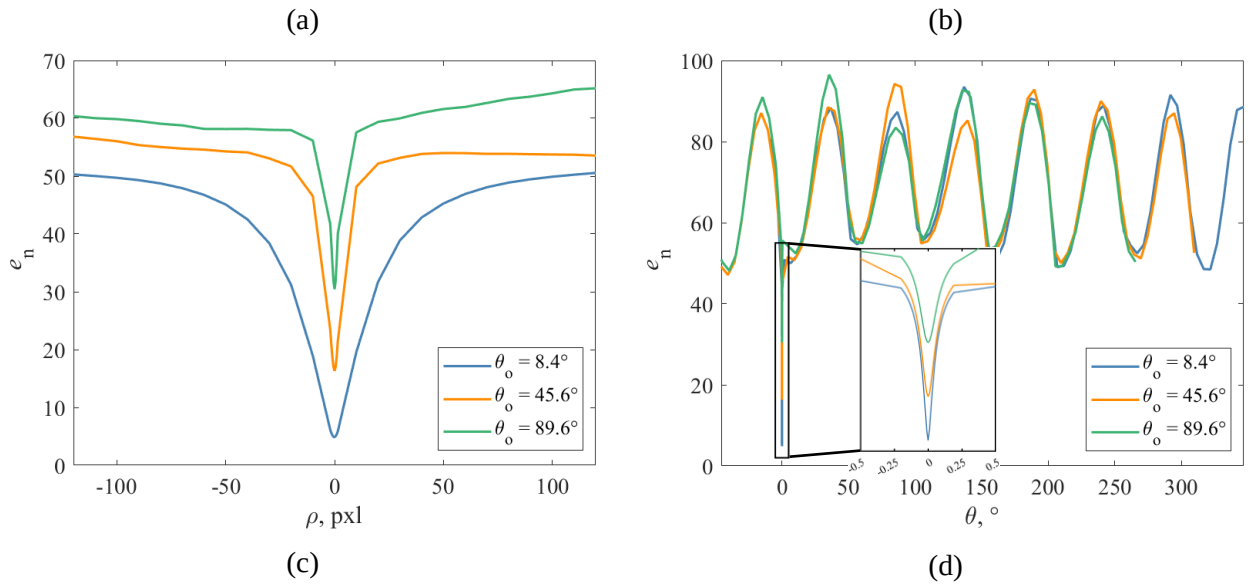

Figure 4 – Exploration of the optimization space: (a) optimization surface for $\theta_o = 8.4°$, (b) zoomed view of the surface for increasing values of θ_o, (c) cross section of the surface with a plane at θ_o, (d) cross section of the surface with a plane at ρ_o.

As shown in Fig. 4(a), the optimization surface exhibits seven local minima along the angular coordinate. This behavior is due to the periodic geometry of the fan: whenever the angle crosses an integer multiple of $360/N_b$ (with N_b denoting the number of blades), a reasonably good correlation is obtained for any value of ρ. However, a global minimum is clearly observed at $\theta = \theta_o$, particularly when ρ approaches $\rho_o = 0$. At the optimal location $[\theta_o, \rho_o]$, the global minimum is reached, characterized by a very sharp trend. To better illustrate this feature, Fig. 4(b) reports the optimization surface for different rotation angles. In Fig. 4, the θ-axis has been shifted so that θ_o corresponds to 0° for ease of comparison. As the rotation angle increases, the final residual error e_n also increases, and the global minimum becomes progressively sharper, requiring a more accurate initial guess to ensure successful optimization. The shape of the global minimum was further investigated through cross-sections of the optimization surface along the planes $\theta = \theta_o$ and $\rho = \rho_o$, shown in Fig. 4(c) and Fig. 4(d), respectively. A zoomed view of the sharp minimum is provided in Fig. 4(d) (black box). The plots highlight that the global minimum is relatively broad along ρ, but extremely sharp along θ. Moreover, the comparison of the three curves in both Figs. 4(c) and (d) confirms that the peak becomes narrower along both ρ and θ as the rotation angle increases. This analysis underlines the necessity of a reliable and robust procedure for selecting the first guess in the optimization. The current three-step approach relies on manual selection of a tentative center of rotation and a computationally expensive *for-loop* search over θ. Two main drawbacks arise: (i) as shown in Fig. 4(c), the optimization surface becomes sharper in the ρ domain as the rotation angle increases, requiring a more precise first guess of the center of rotation, that can be difficult to achieve manually; (ii) the for-loop search is too slow to be applied to every image, especially when multiple repetitions are needed

to refine the initial center estimate. For these reasons, this work introduces a procedure that replaces the unreliable and computationally expensive *for-loop* search.

2.5. Image unwrapping algorithm

To overcome the limitations of the *for-loop* approach and drastically reduce computational time, the circular motion of the rotating object is exploited. Assuming that the center of rotation is known, image unwrapping can be performed to convert the annular region of the fan into a rectangular image. A grid of points is then defined in polar coordinates, with the radial range extending from a minimum and a maximum (i.e. R_m and R_M, respectively) and the angular range spanning 0–360°. Given an arbitrary radial grid step s_r, the corresponding angular step s_θ is expressed in radians such that the arc length at the maximum radius equals s_r:

$$s_\theta = \frac{s_r}{R_M} \tag{9}$$

It should be noted that the spatial resolution of the grid is finer near the center of rotation and becomes coarser as the radius approaches R_M, since the same number of points are placed on each circumference regardless of radius. However, the resolution of the final unwrapped image can be controlled by selecting the radial step s_r. Figure 5(a) illustrates an example of a point grid obtained with a coarse resolution (s_r = 100) for improved readability.

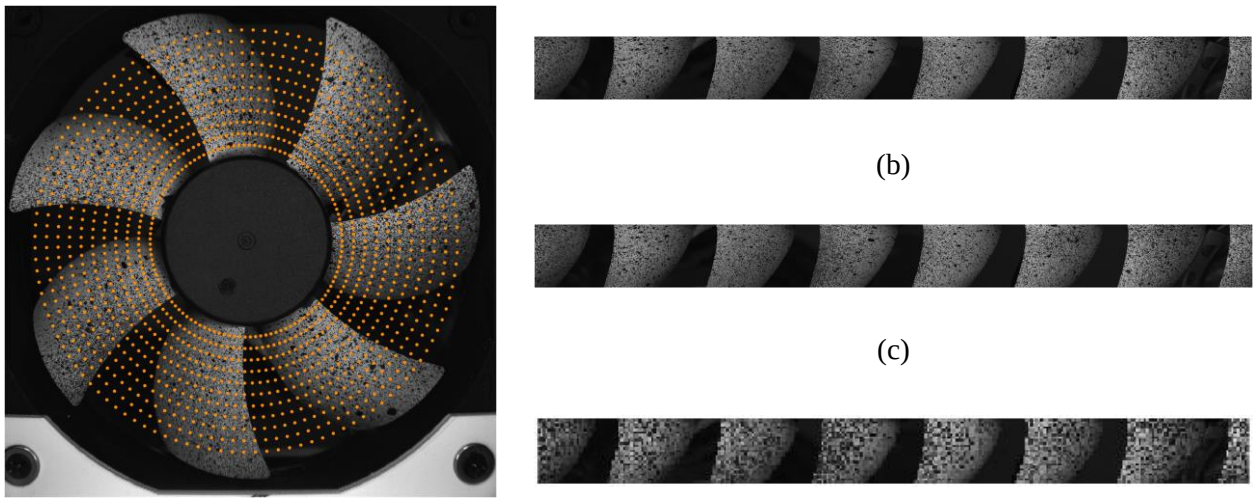

(a) (b) (c) (d)

Figure 5 – Image unwrapping example: (a) definition of the polar point grid. Unwrapped image setting: (b) $s_r = 1$ (c) $s_r = 5$ (d) $s_r = 50$.

Once the grid is defined, bicubic spline interpolation is used to compute the gray-level values of the original image at the grid locations. The synthetic image is then unwrapped by interpreting the radial coordinate as the row index and the angular coordinate as the column index, yielding the image I_S. Due to this transformation,

the rotational displacement of the original image is transformed into a horizontal translational displacement in I_S. Figure 5(b-d) shows three examples of this procedure using s_r = 1, s_r = 5, and s_r = 50. As expected, computational time increases with the number of grid points: the tested resolutions required t_1 = 8.77 s, t_5 = 1.24 s, and t_{50} = 0.74 s, respectively. Although the computational cost remains acceptable even for the finest grid, a trade-off between image resolution and processing time must be achieved, since the unwrapping is embedded in an iterative optimization algorithm. In the following, a value of s_r = 5 was adopted as a suitable compromise.

2.6. Spatial-domain-FFT based DIC

As anticipated in the previous section, once the image is unwrapped, the rotational displacement is transformed into a translational displacement along the horizontal axis. Owing to the cyclic nature of the unwrapping, the image exhibits a wraparound effect, whereby a point leaving one side of the image reappears on the opposite side. This property is fully consistent with the assumptions of spatial-domain FFT-based Digital Image Correlation (DIC) algorithms, which rely on the circular convolution theorem [30]. This approach is typically embedded in local DIC algorithms and applied to image subsets, since the cross-correlation between two signals *u* and *w* can be efficiently computed from their Fast Fourier Transforms *U* and *W* as:

$$C_{\mathrm{fd}} = \frac{\mathrm{ifft}(U^* \cdot W)}{\sqrt{\max(\mathrm{ifft}(U^* \cdot U))\max(\mathrm{ifft}(W^* \cdot W))}} \tag{10}$$

where the function ifft(·) denotes the inverse Fast Fourier Transform, and the operator (·)* denotes the complex conjugate of the argument. This approach was originally applied to image subsets to define a local DIC algorithm in [31]: given an $n \times n$ subset, an $n \times n$ correlation map can be obtained using Eq. 10. The actual displacement is then identified as the location of the maximum in the correlation map. The main limitation of such algorithms is that, at the local level, subsets do not strictly satisfy the periodic boundary conditions, thereby introducing measurement errors, especially for large displacements. Conversely, when the same approach is applied to the entire unwrapped image as described earlier, the periodicity assumption is fulfilled. As a result, the computation remains accurate even in the presence of large horizontal displacements (corresponding to large rotational displacements in the original image). Within this framework, the correlation map is computed between the unwrapped reference image I_{0s} and the unwrapped rotated image I_{1s}. The column of the correlation map associated with the maximum (d_M) is then used to rearrange I_{1s}. Specifically, the array is split into two parts: P_1 includes the columns from 1 to d_M, while P_2 includes the columns from d_M + 1 to the end. The rearranged image $I_{1s,r}$ is then obtained as:

$$I_{1s} = [P_1 \quad P_2]$$
$$I_{1s,r} = [P_2 \quad P_1] \tag{11}$$

The procedure is illustrated in Fig. 6. The first row of the figure shows I_{0s}, with a schematic example on the left and the actual rotating fan on the right. The second row shows I_{1s} in both cases, highlighting the horizontal shift with respect to I_{0s}, which represents the horizontal displacement. The third row shows $I_{1s,r}$, demonstrating that the described procedure successfully realigns $I_{1s,r}$ with I_{0s}. Finally, since each column of $I_{1s,r}$ corresponds to a different angle (depending on the choice of s_θ), the rotation angle between I_{0s} and $I_{1s,r}$ can be directly obtained as $\theta = s_\theta \cdot d_M$.

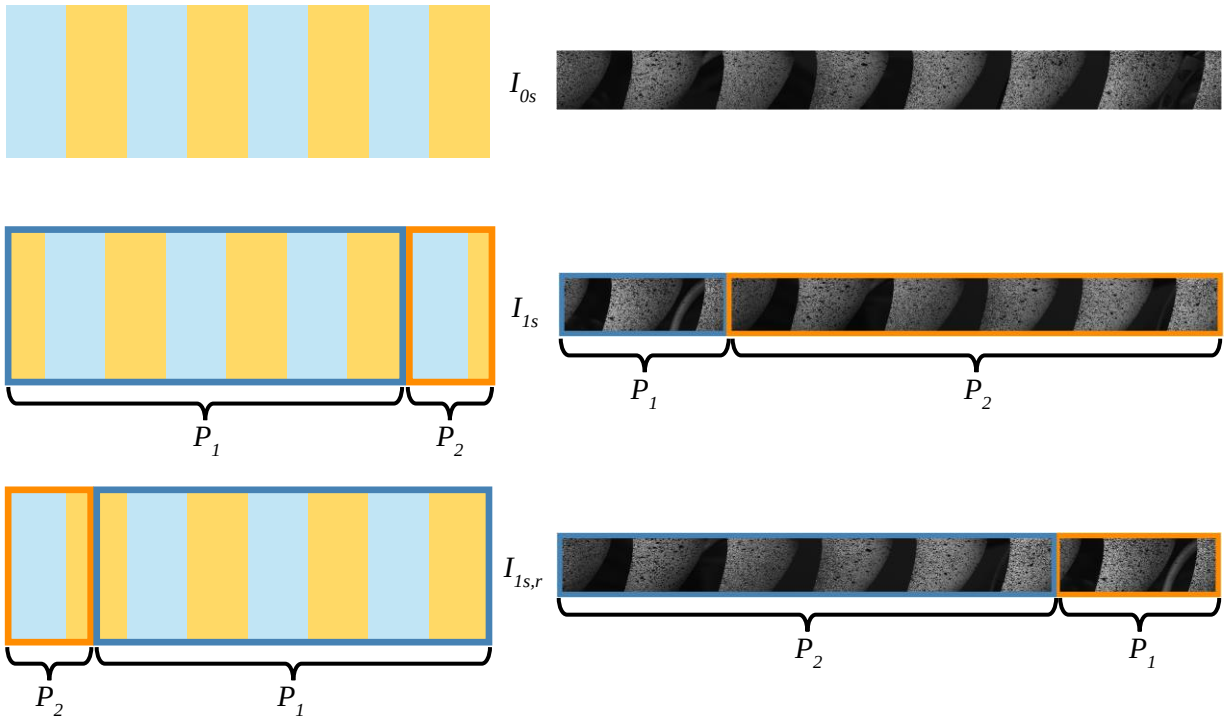

Figure 6 – Unwrapped images elaboration: schematic example (left) and rotating fan example (right).

The described procedure is highly effective in determining the rotation angle once the center of rotation is known. To evaluate the sensitivity of the method with respect to the translation parameter T, the procedure was repeated on the same image pair by exploring a grid of T_1 and T_2 values within ±200 pixels around the optimal solution T_o, and computing e_n for each grid point. This analysis provides insight into the feasibility of embedding the proposed procedure (i.e., image unwrapping combined with spatial-domain FFT displacement computation) within an optimization algorithm to identify the center of rotation. In this framework, the objective function $e_{n,uw}$ is defined as:

$$e_{\mathrm{uw}} = I_{0\mathrm{s}} - I_{1\mathrm{s,r}}$$
$$e_{\mathrm{n,uw}} = \frac{|e_{\mathrm{uw}}|}{\sqrt{n_{e_{\mathrm{uw}}}}} \tag{12}$$

Where $n_{e_{\mathrm{uw}}}$ denotes the number of elements of e_{uw}. The results are shown in Fig. 7, indicating that the optimization function is nearly insensitive to T when far from the optimal location (i.e., beyond approximately ±50 pixels from the minimum), while exhibiting a very sharp peak in the proximity of the optimum.

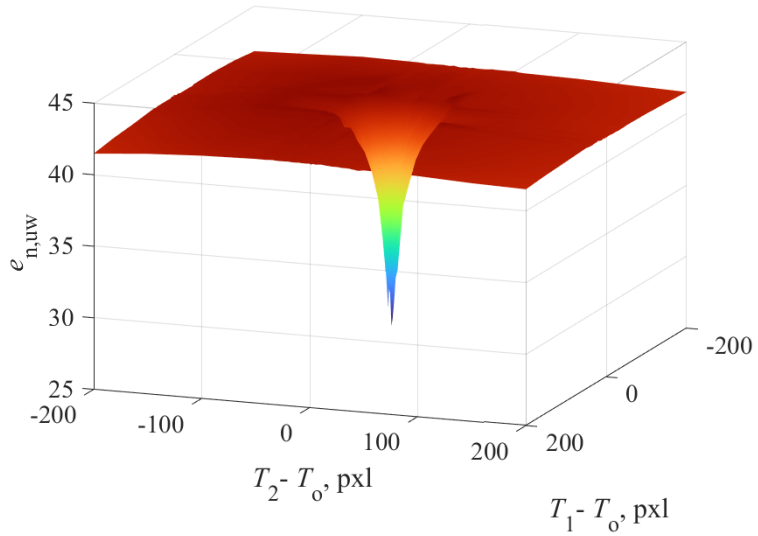

Figure 7 – Optimization surface for the unwrapping / spatial-domain-FFT procedure.

2.7. Center of rotation rough estimation

The proposed algorithm, based on spatial-domain FFT, proves to be highly reliable in estimating the rotation angle, provided that the center of rotation is accurately determined. To obtain such an estimate, a preliminary optimization is performed. The underlying assumption of this procedure is that the unwrapped images exhibit periodicity along the horizontal coordinate, which should hold for every row of the unwrapped image. However, this is true only if the unwrapping is carried out using the correct center of rotation. If the center is misestimated, the resulting unwrapped image loses its periodic nature. This phenomenon is illustrated in Fig. 8: Fig. 8(a) shows a zoomed view of Fig. 5(c), while Fig. 8(b) presents the corresponding unwrapped image where an error of 300 pixels was intentionally introduced along the vertical coordinate of the center. As can be observed, the misestimated center causes the fan blades to appear distorted, thereby highlighting the loss of periodicity. To quantify image periodicity, the FFT of each row of the unwrapped image is computed, after subtracting the mean value of the row to eliminate the amplitude of the zeroth harmonic. Since the number of blades is N_{b}, a peak in the FFT at N_{b} is expected, together with its integer multiples. For improved clarity, the

value A_m is defined by averaging the amplitudes of each harmonic component of the FFT along the rows. This amplitude is then normalized with respect to the sum of the amplitudes across all harmonics. The results are reported in Fig. 8(c) for the cases shown in Fig. 8(a) and Fig. 8(b). The blue curve corresponds to the ideal case of the exact center location (i.e., elaboration of Fig. 8(a)), while the orange curve refers to the case with a significant error in the center estimate (i.e., elaboration of Fig. 8(b)).

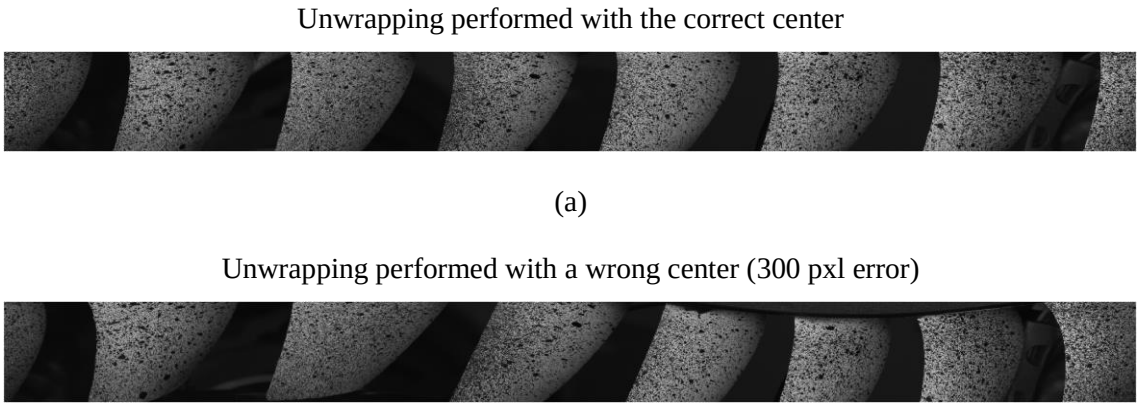

Figure 8 – Row-wise FFT computation: (a) unwrapping with correct center, (b) unwrapping with wrong center (300 pxl error), (c) comparison of the corresponding row-wise FFTs.

The figure shows that the peak of the orange curve is significantly lower than that of the blue curve. In the blue curve, the N_b-th harmonic clearly dominates, together with several of its integer multiples. By contrast, the orange curve exhibits a peak at a frequency different from N_b, with the spectral energy distributed more uniformly across the harmonic indexes and without any dominant peaks. To capture this behavior, a periodicity metric was defined as the sum of the amplitudes of the first ten integer multiples of N_b. Higher values of this

metric indicate stronger periodicity, whereas lower values correspond to a loss of periodicity. To reformulate the problem as a minimization, the sign of this metric was reversed and labeled as *A*, so that the objective function is always negative and the optimization seeks its minimum. The resulting optimization surface is presented in Fig. 9(a). For comparison, the plot was rescaled to match the scale of the optimization surface shown in Fig. 7, which is also included in blue. The newly defined optimization surface exhibits a monotonic trend within the range ±200 pxl, with significant gradients throughout the analyzed region, whereas the blue surface shows almost no gradient outside the ±50 pxl interval. This indicates that the optimization is likely to converge to the true minimum from any initial guess within the ±200 pxl range. Importantly, the comparison of the two surfaces confirms that their minima coincide, thereby validating the use of the proposed periodicity metric for a robust optimization of the center of rotation. To provide a graphical illustration of the performance of the two approaches (i.e. spatial-domain FFT vs row-wise FFT), Fig. 9(b) presents a zoomed view of the blisk, where markers indicate the actual center of rotation (blue dot) and the confidence regions corresponding to ±50 pxl (orange rectangle, spatial-domain FFT) and ±200 pxl (green rectangle, row-wise FFT). Since the green area is relatively large, a suitable first guess can be obtained in various ways, for example by manually selecting a point in the image or by automatically computing the centroid of the white region corresponding to the blades.

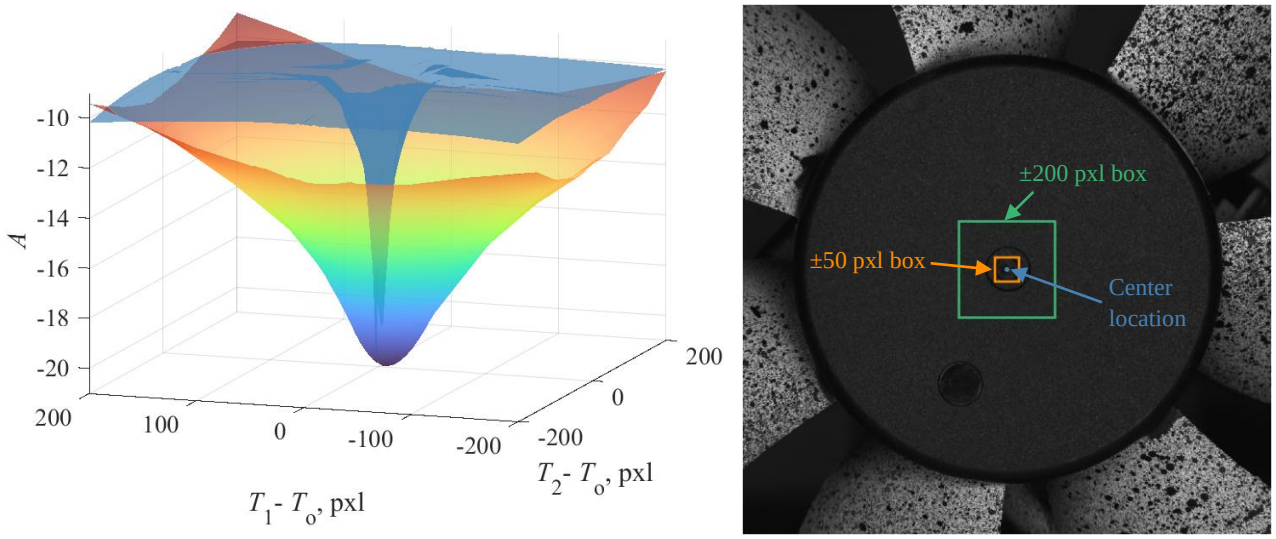

(a) (b)

Figure 9 – Row-wise FFT procedure: (a) optimization surface and (b) confidence boxes.

2.8. Algorithm overview

Due to the nature of the studied optimization problem, the analysis was divided into sub-steps to ensure successful convergence. The main stages of the developed algorithm can be summarized as follows:

1. Image acquisition and initialization: the image is acquired and all derivatives required for bicubic interpolation are computed.
2. First-guess definition: the center of rotation C_0 is manually selected, or alternatively estimated using approximate algorithms (e.g., blade centroid).
3. Row-wise FFT optimization: the row-wise FFT procedure is applied to refine the estimate of the center of rotation, yielding C_1 starting from C_0, and to compute the corresponding translation T_1 (Eq. 2).
4. Image unwrapping and spatial-domain FFT: a single unwrapping operation around C_1 is performed, followed by the spatial-domain FFT procedure, to provide an accurate first estimate of the rotation angle θ_0.
5. Gauss–Newton optimization: planar roto-translation optimization (Eq. 5) is carried out, starting from T_1 and θ_0, to obtain the final translation T_f (and the corresponding center of rotation C_f) and the final optimal rotation angle θ_f.

As previously discussed, the row-wise FFT procedure is significantly more robust to the initial guess of the center location than the image unwrapping procedure. To verify this, the algorithm was executed multiple times with different initial values of C_0. In the first case, the image unwrapping procedure was applied, while in the second case the row-wise FFT procedure was used. The final results T_f and θ_f were compared against the known ground-truth parameters T_O and θ_O (i.e. the minima of the plots in Fig. 4(b), known in these preliminary examples). A performance metric (M_O) was defined as the norm of the difference between the three-element vectors [T_f θ_f] and [T_O θ_O], normalized by the image size (for translation) and 2π (for rotation). In addition, the residual error e_n at the end of the optimization was evaluated to further quantify the agreement between reference and rotated points. The results are reported in Fig. 10, where the color scale represents the performance metric. The top row shows the distribution of M_O, while the bottom row refers to e_n. The plots on the left correspond to the spatial-domain FFT optimization, whereas those on the right correspond to the row-wise FFT procedure. A common color scale was used to directly compare the performance of the two approaches. The results show that the spatial-domain FFT method yields reliable outcomes only when the first guess of the center of rotation lies within ±50 pxl from the optimal value, as already observed in Section 2.6. In this range, both M_O and e_n reach low values, while for larger deviations, performance rapidly deteriorates. Conversely, the row-wise FFT procedure consistently provides low values of both performance metrics across the entire tested range of ±200 pixels.

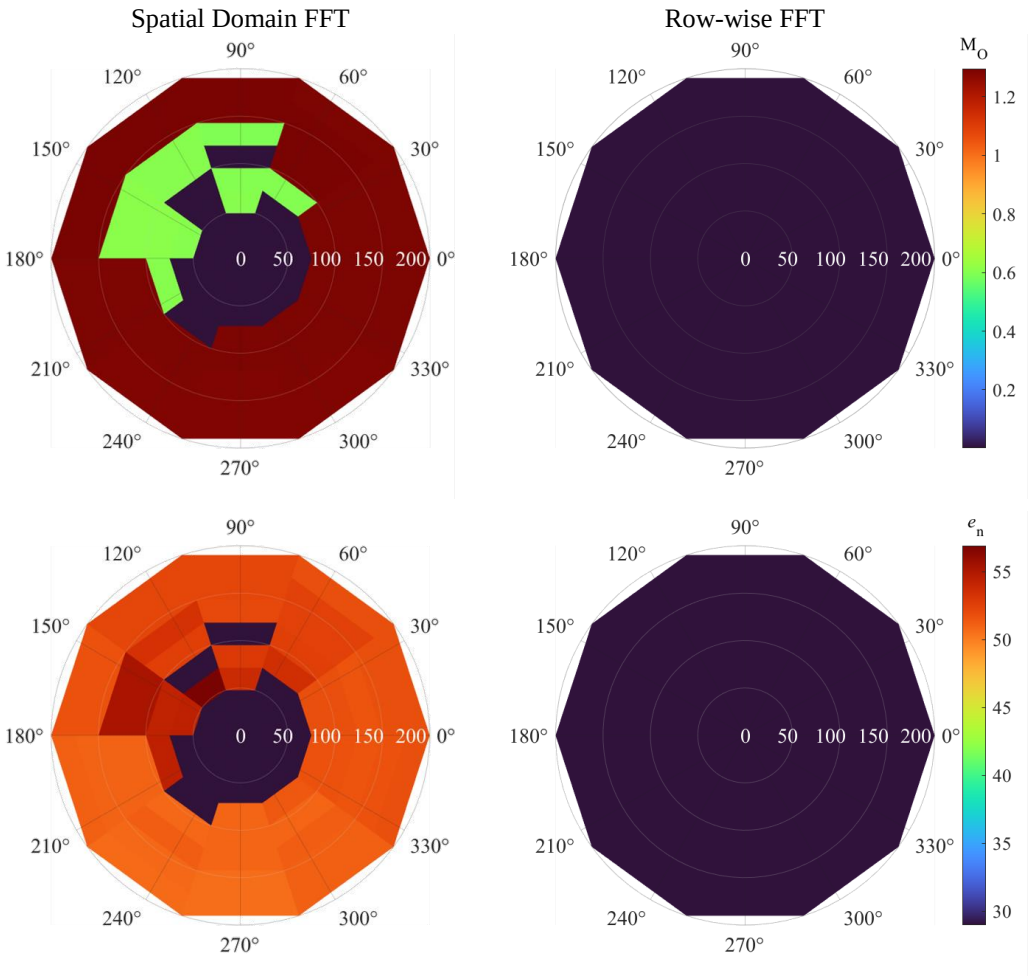

Figure 10 – Performance metrics for the tested algorithms.

To further demonstrate the robustness of the row-wise FFT method to the choice of initial center location, Tab. B reports the mean value (μ) and standard deviation (σ) of both performance metrics obtained with the two algorithms.

Table B – Performance metrics for the considered algorithms

	M_O		e_n	
Algorithm	μ	σ	μ	σ
Spatial-domain FFT	7.703×10^{-1}	5.9×10^{-1}	44.3	10.9
Row-wise FFT	4.1×10^{-3}	1.0×10^{-7}	29.9	3.1×10^{-7}

Inspection of column μ shows that the row-wise FFT approach yields much lower values for both performance metrics. Furthermore, column σ indicates that the row-wise procedure produces nearly identical optimization results for any initial guess of the center location within the tested range, confirming the findings reported in Fig. 10. This analysis demonstrates that the row-wise procedure is the most robust approach for determining the first guess of the center of rotation. Nevertheless, once the center of rotation has been reliably identified

by the row-wise FFT procedure, the spatial-domain FFT algorithm can still be effectively employed to refine the initial guess of the rotation angle.

3. Experimental validation

The proposed procedure was validated using a dataset acquired from a rotating PC fan. A complete revolution was recorded in order to evaluate the performance of the method at increasing rotation angles.

3.1. Measurement setup

A dedicated test bench was designed to carry out the measurements. A steel plate served as the base structure, securely holding the PC fan with a 3D-printed bracket. Several holes were drilled into the plate to allow positioning of a digital camera (Optomotive Smilodon, 5120 × 5120 pxl, 1.1”, 150 fps) at different distances using a custom support. A Computar 05-VL6Z1626UC-MPYIR varifocal lens was mounted on the camera to precisely define the field of view, while a ring light was attached to the lens to ensure uniform illumination of the fan during rotation. An overview of the experimental setup is provided in Fig. 11(a).

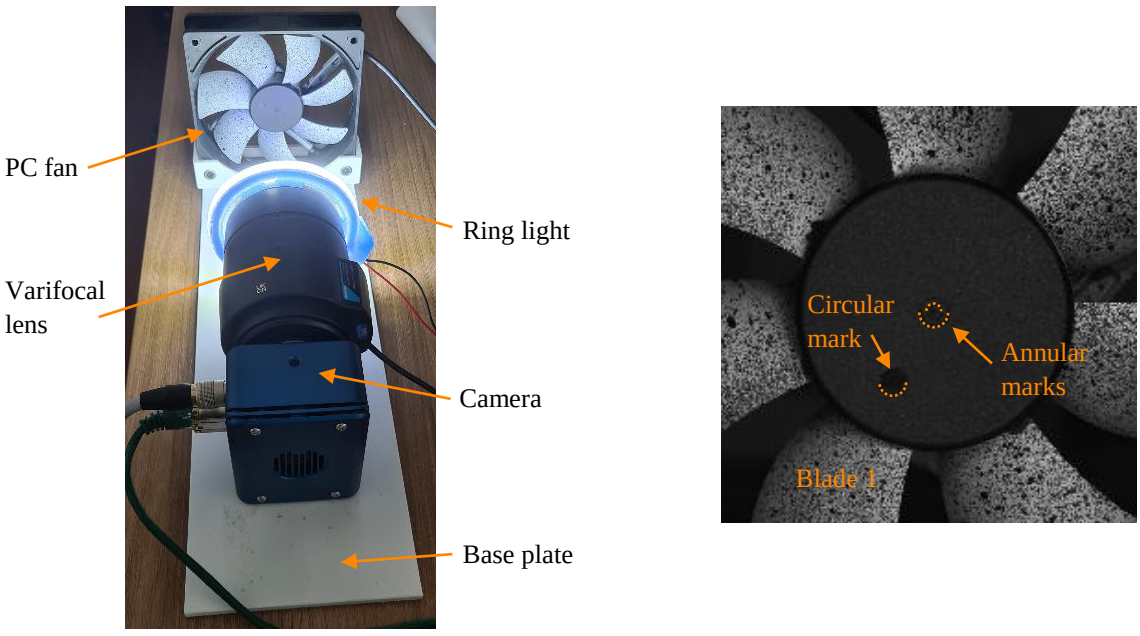

(a) (b)

Figure 11 – Experimental setup: (a) placement of the digital camera and (b) zoomed view of the marks on the blisk.

The fan employed in the experimental setup consists of seven blades with a maximum diameter of approximately 110 mm. It is powered via a standard USB connection, which allows the selection of three discrete rotational speeds: 1000, 1250, and 1500 revolutions per minute (rpm). Two concentric annular marks

are present near the fan center, which are convenient to manually click for a rough estimation of the center of rotation. An additional circular mark is present on the hub, which was used to identify blade number one (see Fig. 11(b)). To ensure that the entire rotor remained within the field of view during operation, the distance between the fan and the optical system was carefully adjusted. The final configuration resulted in a field of view of about 130 × 130 mm², sufficiently wide to capture all blades throughout the full 360° rotation. Since the original blade surface was nearly uniform and dark, a surface preparation procedure was performed to improve optical measurement accuracy. Specifically, the blisk was first coated with a homogeneous white background layer, followed by the application of a high-contrast random speckle pattern using black spray paint. This treatment ensured sufficient texture for digital image correlation and enabled reliable tracking of blade motion.

3.2. Measurement results

The fan was imaged at different angular positions during rotation. It should be noted that no encoder was used in this study to record the rotation angle and that the fan's rotational speed was not precisely controlled. Consequently, images could only be acquired at approximate angular positions rather than at exact values. The reference image was selected when blade number one was nearly vertical in its upper position. Eight additional images were then acquired, approximately evenly spaced over the 360° revolution, i.e., close to 45°, 90°, 135°, 180°, 225°, 270°, 315°, and 360°. If the acquisition angle could have been set precisely, the last image would coincide with the reference image. However, due to the lack of synchronization between the camera and the fan, the final image is expected to display a small angular offset relative to the reference. Table A reports the corresponding results, including the initialization parameters (i.e., tentative center location C_0, manually selected on the reference image) and the optimized values of the center location (C_f) and rotation angle (θ_f). additionally, the total optimization time t_t is reported in the last column of the table, to provide an estimate of the overall computational effort (which drastically reduce with respect to the 60 min for each picture mentioned in Section 2.4).

Table A – Optimization results for different rotation angles

Image #	C_0, pxl	C_f, pxl	θ_f, °	$\theta_{f,r}$, °	e_n, pxl	$\bar{e}$, pxl	t_t, s
1	[2511 2407]	[2509.1 2410.6]	48.98	48.98	8.98	7.00	34.9
2		[2507.8 2410.8]	84.18	84.18	12.28	9.49	22.1
3		[2508.0 2410.9]	132.52	132.52	16.25	12.80	30.4
4		[2508.0 2410.2]	176.97	176.97	18.41	14.78	30.2
5		[2507.1 2409.6]	215.14	-144.86	19.76	16.08	40.4
6		[2505.2 2408.8]	268.52	-91.48	19.14	15.40	45.0
7		[2503.0 2409.4]	303.98	-56.02	14.21	11.28	30.9
8		[2482.9 2410.2]	351.16	-8.84	3.71	2.95	20.4

Additionally, the value $\theta_{f,r}$ was defined by rearranging the values of θ_f as follows:

$$\begin{cases} \theta_{f,r} = \theta_f & \text{if } \theta_f \leq 180° \\ \theta_{f,r} = \theta_f - 360° & \text{if } \theta_f > 180° \end{cases} \quad (13)$$

This procedure was adopted to avoid ambiguities between positive and negative rotation angles when sorting them in ascending order. For example, a rotation angle of 350° may appear larger than a rotation angle of 170°, while in practice it corresponds to a small negative rotation of −10°. To further assess the optimization performance, additional metrics were computed from the error vector e defined in Section 2.1. Specifically, the scalar e_n (as defined in Section 2.4) and the mean absolute error $\bar{e} = \sum|e| / n_e$ (the operator $|\,.\,|$ represents the absolute value of the argument, while n_e again represents the number of elements in e) were evaluated for each rotation angle. As expected, Table A indicates that the estimated center of rotation C_f remains stable across frames, with only minor variations on the order of 5 pixels. Considering the field of view and camera resolution, these oscillations correspond to approximately 0.12 mm and can be attributed to small vibrations of the measurement system and of the hub itself. To better illustrate the correlation between the rotation angle and the optimization results, the last two columns of Table A are plotted in Fig. 12 against $\theta_{f,r}$.

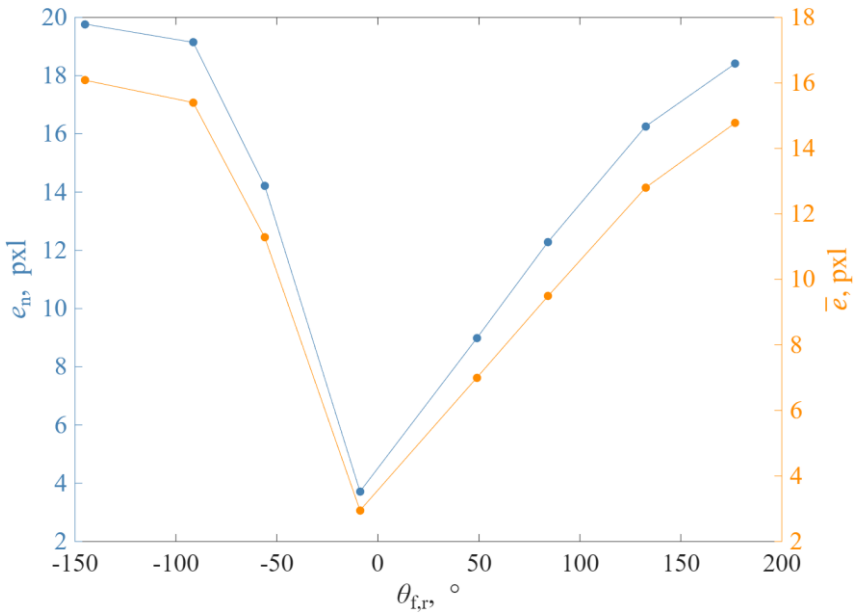

Figure 12 – Correlation between rotation angle and optimization outcomes

The plot shows a similar trend for both e_n and $\bar{e}$, with larger errors observed at higher rotation angles, and a minimum reached near 0°. This behavior can be explained by optical distortions caused by unavoidable misalignments between the camera and the fan: when the sensor plane is not perfectly aligned with the rotor plane, a perfect circle is perceived as an ellipse during rotation, while the rotation model defined in Eq. 1 only accounts for a rigid body rotation. To validate this observation, the point grid used for the optimization was roto-translated by T_f and θ_f and superimposed on the corresponding image. For a clearer comparison across

different rotation angles, the resulting images were de-rotated so that blade number one always appeared in the same position as in the reference image. Two zoomed regions were then analyzed: one close to the blade root and the other close to the blade tip. Since only the informative pixel at the speckle edges were retained in the optimization (as described in Section 2.3), these plots allow direct assessment of whether the rotated point grid aligns correctly with the corresponding rotated speckles. The results of this comparison are reported in Fig. 13. The top image corresponds to the reference configuration, with a blue box indicating the zoomed view of a speckle near the blade root and an orange box showing a speckle near the blade tip. The bottom-left image presents the results for $\theta_{f,r}$ = 8.84°, where the rotated point grid aligns well with the speckle edges in both the root and tip regions. By contrast, the bottom-right image refers to $\theta_{f,r}$ = −144.86°, showing good agreement between the point grid and the speckle edge in the region near the root, but a noticeable misalignment at the blade tip. These observations demonstrate that, at large rotation angles, optical distortions of the fan hinder the ability of the optimization procedure to accurately match all speckles, leading to higher residual errors. It should be noted, however, that this effect does not compromise the optimization process itself, since the resulting solution still provides a valid representation of the fan's roto-translation. Nonetheless, such distortions could potentially be mitigated by employing a stereo-camera system, which would exploit 3D information to compensate for perspective effects.

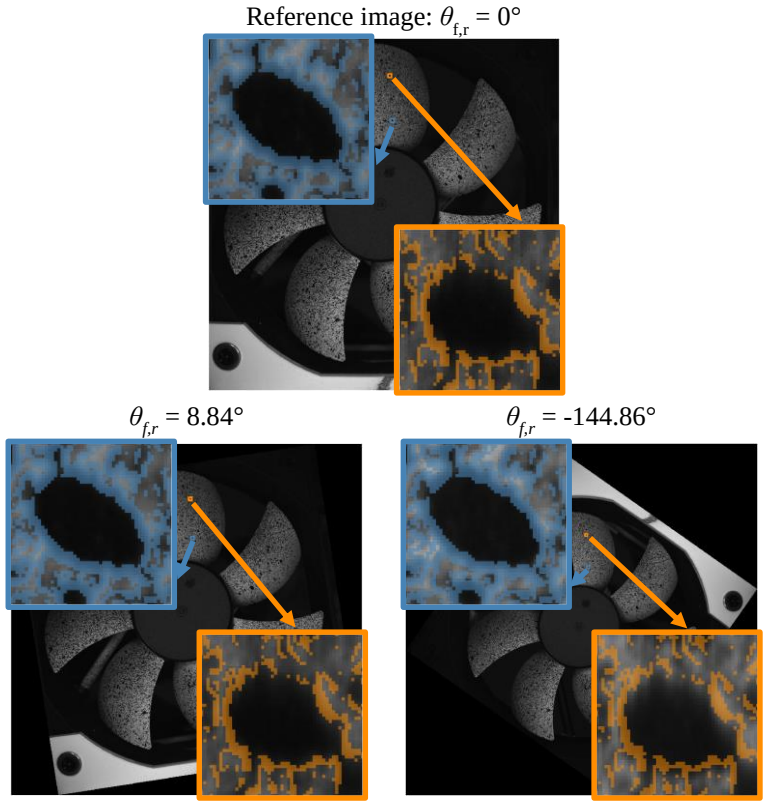

Figure 13 – Alignment of the rotated point grid with the speckle pattern at selected angles (reference, $\theta_{f,r}$ = 8.84°, $\theta_{f,r}$ = -144.86°); zoomed views at blade root and tip

4. Conclusions

This work presents a novel global Digital Image Correlation (DIC) algorithm tailored for tracking the rigid-body motion of rotating objects. By combining circular image unwrapping, spatial-domain FFT analysis, and row-wise FFT optimization, the proposed method transforms rotational displacements into linear shifts, enabling a robust initial estimation of rotation parameters. A Gauss–Newton optimization scheme is then employed to refine these estimates by minimizing pixel-wise intensity errors across selected regions of interest. To improve computational efficiency, a sensitivity-based pixel selection strategy is adopted, retaining only the most informative pixels along speckle edges while discarding those in uniform regions. This approach significantly reduces the dataset size and accelerates convergence, further enhancing the accuracy. Experimental validation on a rotating PC fan demonstrated the method's ability to track full 360° rotations with high precision. After image unwrapping, the center of rotation was reliably estimated using a row-wise FFT periodicity metric, which proved high robustness even under large angular displacements. The first guess for the rotation angle was then obtained using a spatial-domain FFT algorithm, before final refinement through Gauss–Newton optimization based on an analytical roto-translation model.

Overall, the proposed method provides a computationally efficient and accurate solution for full-field optical measurement of rotating structures (the overall computational time is in the range 30-40 s for each image), with promising applications in vibration analysis, modal testing, and condition monitoring. Some limitations remain: optical distortions due to misalignment between the camera and rotor plane may reduce matching performance at large rotation angles, and the current implementation assumes rigid-body motion, neglecting out-of-plane deformations or perspective effects. These issues could be mitigated in future work by integrating stereo-camera systems or extending the model to account for non-rigid transformations induced by vibrations or optical distortions.

References

[1] S.L.D. Shah, M.C. Luintel, S. Bhattrai, Comprehensive review on vibration response and dynamic analysis of rotating blades under thermal environment, Int J Dynam Control, 13 (2025).
[2] S. Boedecker, A. Dräbenstedt, L. Heller, A. Kraft, A. Leonhardt, C. Pape, S. Ristau, E. Reithmeier, C. Rembe, Optical derotator for scanning vibrometer measurements on rotating objects, Seventh International Conference on Vibration Measurements by Laser Techniques: Advances and Applications, 6345 (2006).
[3] D. Di Maio, D.J. Ewins, Applications of continuous tracking SLDV measurement methods to axially symmetric rotating structures using different excitation methods, Mech Syst Signal Pr, 24 (2010) 3013-3036.
[4] P. Castellini, N. Paone, Development of the tracking laser vibrometer: Performance and uncertainty analysis, Rev Sci Instrum, 71 (2000) 4639-4647.
[5] H. Khalil, D. Kim, Y. Jo, K. Park, Optical derotator alignment using image-processing algorithm for tracking laser vibrometer measurements of rotating objects, Rev Sci Instrum, 88 (2017).
[6] B. Altmann, T. Betker, C. Pape, E. Reithmeier, Alignment strategy for an optomechanical image derotator using a laser Doppler vibrometer, Appl Optics, 58 (2019) 6555-6568.
[7] L.F. Lyu, W. Zhu, D.T. Will, K. Yuan, A novel misalignment angle correction method for vibration measurement of a rotating structure using an image-based tracking continuously scanning laser Doppler vibrometer, Opt Laser Technol, 190 (2025).

[8] M. Ozbek, D.J. Rixen, O. Erne, G. Sanow, Feasibility of monitoring large wind turbines using photogrammetry, Energy, 35 (2010) 4802-4811.
[9] T. Lundstrom, J. Baqersad, C. Niezrecki, Using High-Speed Stereophotogrammetry to Collect Operating Data on a Robinson R44 Helicopter, in: R. Allemang, J. De Clerck, C. Niezrecki, A. Wicks (Eds.) Special Topics in Structural Dynamics, Volume 6, Springer New York, New York, NY, 2013, pp. 401-410.
[10] B.K. Gwashavanhu, A.J. Oberholster, P.S. Heyns, Turbomachinery blade behaviour analysis using a photogrammetric stereovision 3D based shape analysis approach, Opt Laser Eng, 186 (2025).
[11] G. Tohti, Z.Q. Wu, F. Turhun, M. Geni, S. Liu, Dynamic mode measurement method of wind turbine blade based on binocular photogrammetry, Signal Image Video P, 19 (2025).
[12] R. Wu, D.S. Zhang, Q.F. Yu, Y.X. Jiang, D. Arola, Health monitoring of wind turbine blades in operation using three-dimensional digital image correlation, Mech Syst Signal Pr, 130 (2019) 470-483.
[13] Y. Wang, Z. Gao, Z. Fang, Y. Su, Q. Zhang, Rotating Vibration Measurement Using 3D Digital Image Correlation, Exp Mech, 63 (2023) 565-579.
[14] Z. Fang, Y. Gao, Z.R. Gao, Y. Liu, Y.R. Wang, Y. Su, Q.C. Zhang, Efficient and automated initial value estimation in digital image correlation for large displacement, rotation, and scaling, Appl Optics, 59 (2020) 10523-10531.
[15] A. Pilch, A. Mahajan, T. Chu, Measurement of whole-field surface displacements and strain using a genetic algorithm based intelligent image correlation method, J Dyn Syst-T Asme, 126 (2004) 479-488.
[16] J.Q. Zhao, P. Zeng, L.P. Lei, Y. Ma, Initial guess by improved population-based intelligent algorithms for large inter-frame deformation measurement using digital image correlation, Opt Laser Eng, 50 (2012) 473-490.
[17] D. Minervini, D. Mastrodicasa, T. Geluk, E.D. Lorenzo, Novel methodology for isolating rotational phenomena in tire testing, INTER-NOISE and NOISE-CON Congress and Conference Proceedings, 268 (2023) 1845-1856.
[18] R. Hunady, P. Pavelka, P. Lengvarsky, Vibration and modal analysis of a rotating disc using high-speed 3D digital image correlation, Mech Syst Signal Pr, 121 (2019) 201-214.
[19] S. Occhipinti, D. Mastrodicasa, S. Manzato, E. Di Lorenzo, Application of digital image correlation in operational modal analysis of rotating structures, Proceedings of ISMA 2024 - International Conference on Noise and Vibration Engineering and USD 2024 - International Conference on Uncertainty in Structural Dynamics, 2024, pp. 2544-2555.
[20] T. Masmeijer, E. Habtour, K. Zaletelj, J. Slavic, Directional DIC method with automatic feature selection, Mech Syst Signal Pr, 224 (2025).
[21] X.C. Zhang, J.L. Chen, Z.T. Wang, N. Zhan, R.C. Wang, Digital image correlation using ring template and quadrilateral element for large rotation measurement, Opt Laser Eng, 50 (2012) 922-928.
[22] P. Xie, Z.R. Lu, G. Lin, W. Li, L. Wang, A Ring-Projection-Based Two-Scale Approach for Accurate Digital Image Correlation of Large Translations and Rotations, Exp Mech, 64 (2024) 875-893.
[23] L.P. Wang, S.L. Bi, X. Lu, Y.G. Gu, C. Zhai, Deformation measurement of high-speed rotating drone blades based on digital image correlation combined with ring projection transform and orientation codes, Measurement, 148 (2019).
[24] L.P. Wang, S.L. Bi, H. Li, Y.G. Gu, C. Zhai, Fast initial value estimation in digital image correlation for large rotation measurement, Opt Laser Eng, 127 (2020).
[25] J.W. Gu, G. Liu, Q.S. Yang, S.S. Law, Improved SURF method in digital image correlation for estimation of large rotation angle, Measurement, 207 (2023).
[26] F. Zhong, C. Quan, Digital image correlation in polar coordinate robust to a large rotation, Opt Laser Eng, 98 (2017) 153-158.
[27] P. Neri, A. Paoli, A.V. Razionale, S. Barone, Enhanced subpixel sensitivity in 3D-DIC via Spline-Based correlation map interpolation for vibration measurements, Optics & Laser Technology, 188 (2025) 112958.
[28] J. Nocedal, S.J. Wright, Numerical Optimization, Springer New York, NY, 2006.
[29] Å. Björck, Numerical Methods for Least Squares Problems, Siam, Philadelphia 1996.
[30] P. Stoica, R.L. Moses, Spectral analysis of signals, Upper Saddle River, 2005.
[31] P. Neri, A. Paoli, S. Occhipinti, C.M. Firrone, D. Botto, Local digital image correlation algorithms: spatial domain versus frequency domain approach, Proceedings of ISMA 2024 - International Conference on Noise and Vibration Engineering and USD 2024 - International Conference on Uncertainty in Structural Dynamics, 2024, pp. 2411-2420.

Declaration of interests

☒The authors declare that they have no known competing financial interests or personal relationships that could have appeared to influence the work reported in this paper.

☐The authors declare the following financial interests/personal relationships which may be considered as potential competing interests: